https://doi.org/10.20965/ijat.2020.p0552

Paper:

Effects of Pulse Duration and Heat on Laser-Induced Periodic Surface Structures

Shuhei Kodama*,†, Keita Shimada, Masayoshi Mizutani**, and Tsunemoto Kuriyagawa****

*Tokyo University of Agriculture and Technology
2-24-16 Nakacho, Koganei, Tokyo 184-0012, Japan
†Corresponding author, E-mail: shuhei-kodama@go.tuat.ac.jp
**Tohoku University, Sendai, Japan

[Received December 27, 2019; accepted April 3, 2020]

Compared with traditional nanotexturing methods, an ultrashort-pulsed laser is an efficient technology of fabricating nanostructures called laser-induced periodic surface structures (LIPSS) on material surfaces. LIPSS are easily fabricated when the pulse duration is shorter than collisional relaxation time (CRT). Accordingly, ultrashort-pulsed lasers have been mainly used to study LIPSS, but they unstably irradiate while requiring high costs. Although long-pulsed lasers have low cost and high stability, the phenomena (such as the effect of pulse duration, laser wavelength, and heat) of the LIPSS fabricated using short-pulsed lasers with the pulse duration close to the maximum CRT, which is greater than femtosecond, have not been clarified. However, the nanosecond pulse laser has been reported to produce LIPSS, but those were unclear and ununiform. In this study, the short-pulsed laser with the pulse duration of 20 ps, which is close to the maximum CRT, was employed to clarify the effects of pulse duration and heat on the fabrication of LIPSS and to solve problems associated with ultrashort-pulsed lasers. First, a finite-difference time-domain simulation was developed at 20-ps pulse duration to investigate the effects of irradiation conditions on the electric-field-intensity distribution. Subsequently, experiments were conducted using the 20-ps pulse laser by varying conditions. The aspect ratio of the LIPSS obtained was greater than that of the LIPSS fabricated using ultrashort-pulsed lasers, but LIPSS were not fabricated at 355- and 266-nm laser wavelength. In addition, the short-pulsed laser experienced thermal influences and a cooling material was effective for the fabrication of LIPSS with high-aspect-ratio. This demonstrates the effects of pulse duration close to the CRT and heat on the fabrication of LIPSS.

Keywords: short-pulsed laser, 20-ps pulse duration, electric field, laser wavelength, material temperature

1. Introduction

Micro/nanostructures can be used to alter the material-surface functionalities such as tribology [1, 2], wettability [3], optical properties [4], and bioaffinity [5]. Compared with traditional methods, the ultrashort-pulsed laser is more appropriate method of fabricating fine structures, and it is used to fabricate fine periodic structures called laser-induced periodic surface structures (LIPSS). In addition, LIPSS offered functionalities such as the friction reduction [6], water repellency [7], anti-reflection [8], and bioaffinity [9]. Notably, LIPSS are easily fabricated when the pulse duration is shorter than the collisional relaxation time (CRT) from a few ps to approximately 20 ps, as thermal effects occur after CRT [10]. Accordingly, an ultrashort-pulsed laser with the pulse duration of less than 10 ps has been mainly used to study LIPSS, although the lasers with longer pulse duration have lower cost and higher stability [11–13].

Theoretically, it is difficult to fabricate LIPSS by using the nanosecond pulse laser with the wavelength of 1064 nm because of thermal effects and low intensity, however, it produced unclear LIPSS partially [14]. In addition, it has been unclear whether a short-pulsed laser with short laser wavelength can be used to fabricate LIPSS, while an ultrashort-pulsed laser with short laser wavelength can be used to fabricate LIPSS [15–17]. Moreover, LIPSS fabricated at higher temperature had low roughness and threshold. In addition, laser irradiation at high material temperature facilitated the fabrication of LIPSS depending on the material, owing to the increase in the initial carrier density, laser absorption and electron scattering [14, 18–21], although non-thermal processing is effective for fabrication of LIPSS [10]. However, the phenomena associated with the LIPSS fabricated using a short-pulsed laser with pulse duration close to CRT have not been clarified.

The objective of this study is to verify the effects of the pulse duration that is close to CRT, and also analyze the effects of heat on the fabrication of LIPSS, by using a short-pulsed laser with the pulse duration of 20 ps, which is close to the maximum CRT. We also aim to stably fabricate uniform LIPSS on the entire irradiated surface at low cost. First, a finite-difference time-domain (FDTD) simu-

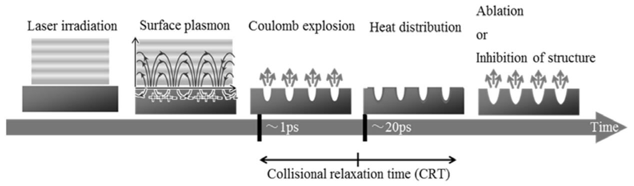

Source: IJAT, Vol.12, No.6 [27], Precision Engineering, Vol.55 [28]

Fig. 1. Processing model of a short-pulsed laser.

lation was conducted with the pulse duration of 20 ps by using a 304 stainless steel material (SUS304, classified by Japanese Industrial Standards), which is a commonly used industrial material, to investigate the effects of conditions on the electric-field-intensity distribution and the geometry of LIPSS when the pulse duration was 20 ps, as laser fluence and wavelength change the electric-field-intensity distribution and electron density related to the pitch length and height of LIPSS [22, 23]. Subsequently, experiments were conducted using the short-pulsed laser with the pulse duration of 20 ps by irradiating on SUS304 substrates while varying the laser energy density, pulse, laser wavelength, and material temperature to investigate the effects of the pulse duration of 20 ps and material temperature on the fabrication and geometry (e.g., pitch length and height) of LIPSS, compared with ultrashort pulsed lasers.

2. Principle

The incident light is divided into plasma waves and scattered lights via protrusions on a surface based on the parametric decay [14, 24–26]. The interference between the incident light and plasma waves induced surface plasmons, resulted in periodic Coulomb explosions on the surface, as depicted in **Fig. 1** [27, 28]. After varying the CRT from a few ps to approximately 20 ps, thermal effects induced the ablation or inhibition of structures, and LIPSS were fabricated. The pitch length of LIPSS on metals is approximately 0.5–0.85 times as long as the laser wavelength and increases upon increasing the laser energy density. Because a laser with pulse duration shorter than CRT can be used to fabricate LIPSS without thermal effects [29], a short-pulsed laser with the pulse duration of 20 ps was employed in this study, as 20 ps is close to the maximum CRT and, therefore, it may induce thermal effects to clarify the effects of 20-ps pulse duration and heat on the fabrication of LIPSS and to stabilize laser irradiation at low cost.

3. FDTD

The principle stated that the pitch length of LIPSS mainly depends on the laser wavelength and that it expands upon increasing the energy density. The electromagnetic field analysis using the FDTD method was performed with various laser intensities and wavelengths to investigate the effects of laser-irradiation conditions (e.g., laser intensity and wavelength) on the electric-field-intensity distribution related to the geometry of resultant LIPSS in the case of the laser with the pulse duration of 20 ps. The 20-ps pulsed laser has thermal effects, which results in the melting and oxidation of the irradiated material surface because of the pulse duration being close to CRT. Notably, CRT expands by lowering the material temperature because the electron-phonon interactions are suppressed. Therefore, laser irradiation with a cooling material was proposed to suppress the thermal effects and easily fabricate sharp LIPSS, which were similar to those fabricated using the femtosecond laser. In addition, the FDTD simulation was performed by varying the material temperature to investigate the effects of material temperature on the electric-field-intensity distribution and fabrication of LIPSS.

3.1. Method

The FDTD simulation is used to indicate electric-field-intensity distribution. The electromagnetic-field intensity is calculated by solving the time-dependent Maxwell's equations, introduced by Yee in 1966 [30, 31]. The time arrangement is determined using Eqs. (1) and (2) as follows:

$$E^n = \frac{1-\dfrac{\sigma\Delta t}{2\varepsilon}}{1+\dfrac{\sigma\Delta t}{2\varepsilon}}E^{n-1}+\frac{\dfrac{\Delta t}{\varepsilon}}{1+\dfrac{\sigma\Delta t}{2\varepsilon}}\nabla\times H^{n-\frac{1}{2}} \quad . \quad (1)$$

$$H^{n+\frac{1}{2}} = H^{n-\frac{1}{2}} - \frac{\Delta t}{\mu}\nabla\times E^n \quad . \; . \; . \; . \; . \; . \; . \quad (2)$$

E denotes the electric field, H the magnetic field, μ the permeability, ε the permittivity, σ the conductivity, superscript n the time steps, and Δt the time increment.

3.2. Analytical Setup and Conditions

Electromagnetic-field analysis with an FDTD simulation (nanophotonic FDTD simulation software from Lumerical Inc.) was performed to investigate the changes in the electric-field-intensity distribution by varying the laser intensity, laser wavelength, and material temperature, depending on the refractive index and extinction coefficient of material, and also to investigate the effects of 20-ps pulse duration and heat on LIPSS fabrication. In **Fig. 2**, we depict the analytical model: the analysis area is the inside of the rectangle represented using the thick line; the monitor area is the inside of a square represented using the thin line; the direction of the incident light is denoted by the arrow, and the direction of the laser polarization is denoted by the double-headed arrow. The surface with grooves was prepared to imitate the case of fabricating LIPSS, as the electric field was homogeneously distributed on the flat surface, meaning the entire surface is removed. The analytical conditions are listed in **Table 1**. The refractive index and extinction coefficient of

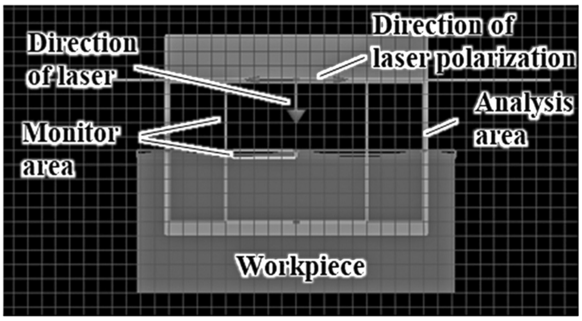

Fig. 2. Analytical model.

Table 1. Analytical conditions.

Laser wavelength	900, 532, 355, 266 nm
Pulse duration	20 ps
Material	SUS304
Pitch length P_g	100–900 nm
Depth	50 nm
Relative intensity	1.0, 2.0, 3.0, 4.0
Material temperature	293, 373 K

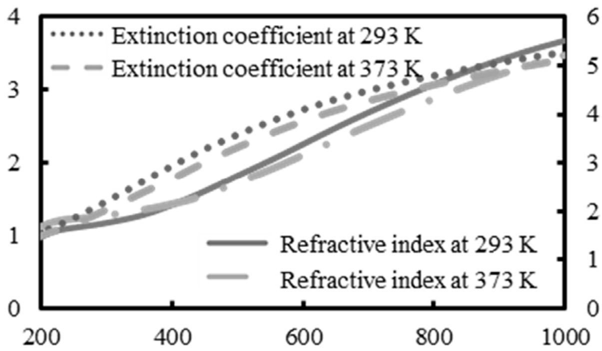

Fig. 3. Refractive index and extinction coefficient of SUS304.

SUS304 were preliminarily measured using an ellipsometer from the wavelength of 200 to 1000 nm at 293 K and 373 K, as depicted in **Fig. 3**. First, the laser wavelength and laser-pulse duration were set to 900 nm and 20 ps, respectively. The depth and pitch length of the grooves were set to 50 and 850 nm, respectively, as the pitch length of LIPSS was close to the laser wavelength. The relative intensities were set to 1.0, 2.0, 3.0, and 4.0. Next, the laser wavelengths were set to 900, 532, 355, and 266 nm, and the pitch lengths of the grooves were set to 700–900, 400–500, 250–350, and 150–250 nm, respectively. Subsequently, the pitch lengths of the grooves were set to 850, 400, 300, and 150 nm for the cases of 900, 532, 355, and 266 nm laser wavelength, respectively. The material temperatures were set to 293 K and 373 K, and the changes in the electric-field intensity were investigated by decreasing the temperature.

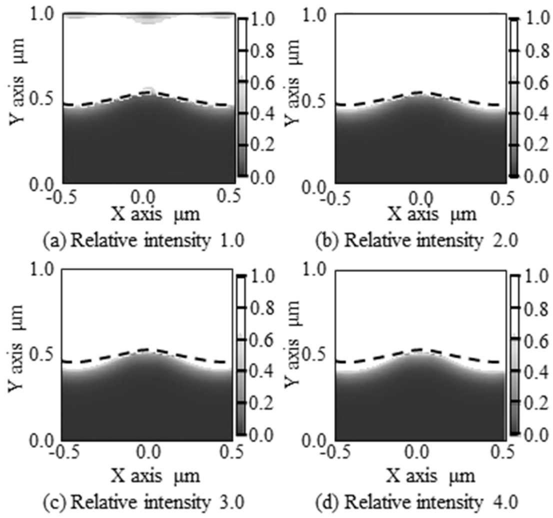

Fig. 4. Electric field distribution at different intensity.

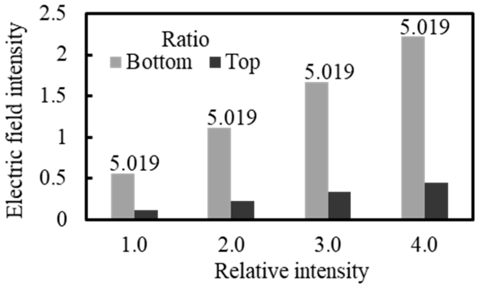

Fig. 5. Relationship between relative intensity and electric field intensity (the number in the figure is the ratio of the electric-field intensity at the bottom of the groove to that at the top of the groove).

3.3. Analytical Results

3.3.1. Simulation with Various Intensities

In **Fig. 4**, we depict the analytical results of electric-field distribution at different intensity with the same scale of electric-field intensity. The upper and lower regions divided using the dotted lines represent the atmosphere and material, respectively. Ablation might occur at the region with large electric-field intensity because of the Coulomb explosion. In the case wherein the penetration depth of the electric field is higher at the bottoms of the grooves than that at the tops of grooves, the bottoms of the grooves might be removed, thereby resulting in LIPSS. The penetration becomes deeper upon increasing the relative intensity, and the electric-field distribution was homogeneously observed on the entire surface at high relative intensity, removing the entire surface. In **Fig. 5**, we depict the changes in the electric-field intensity of top and bottom of the grooves and the ratio of the electric-field intensity at the bottom of groove to that at the top of groove for each relative intensity. The electric-field intensity at the bottoms of grooves slightly increased upon increasing the relative intensity without change in the ratio of the

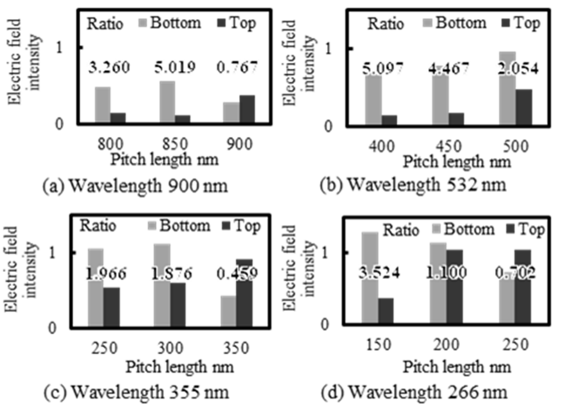

Fig. 6. Relationship between laser wavelength and electric field intensity (the number in the figure is the ratio of the electric-field intensity at the bottom of the groove to that at the top of the groove).

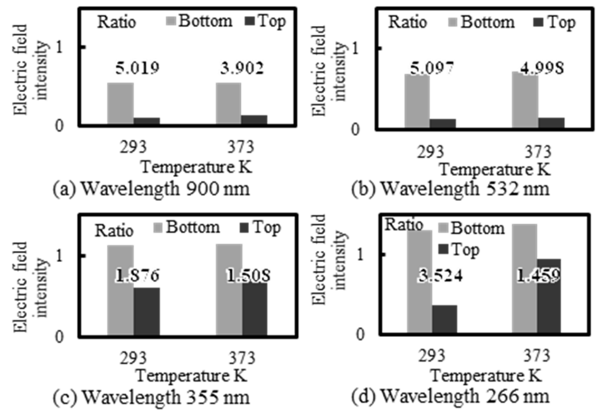

Fig. 7. Relationship between the material temperature and electric-field intensity (number in the figure is the ratio of the electric-field intensity at the bottom of groove to that at the top of groove).

electric-field intensity. The pitch length of the grooves with high ratio was extended with increase in the relative intensity; i.e., the increase in the energy density extends the pitch length of LIPSS, in accordance with the principle of extending the pitch length upon increasing the energy density related to the electric field.

3.3.2. Simulation with Various Laser Wavelengths

In **Fig. 6**, we depict the changes in the electric-field intensity for each laser wavelength. The ratio of the electric-field intensity at the top of the grooves to that at the bottoms of the grooves for the pitch lengths of 850, 400, 300, and 150 nm were large for the laser wavelengths of 900, 532, 355, and 266 nm, respectively, indicating that the laser wavelength mainly determines the pitch length of LIPSS. Moreover, the electric-field intensity increased at both the top and the bottom of the groove upon decreasing the laser wavelength, indicating that shorter-wavelength lasers require lower energy density to fabricate LIPSS, owing to the removal of the entire irradiated surface because of high intensity.

3.3.3. Simulation with Various Material Temperatures

In **Fig. 7**, we depict the changes in the electric-field intensity for each laser wavelength and material temperature. High electric-field intensity was observed on the workpiece surface, especially at the top of the groove, at high material temperature. This indicates that although the threshold decreases, yet the fabrication of LIPSS is difficult at high temperatures because of the removal of the entire irradiated surface. However, the ratio of the electric-field intensity at the bottom of the groove to that at the top of the groove increased for lower material temperatures, indicating that it is easy to fabricate LIPSS with higher aspect ratio (i.e., the height of LIPSS divided by the pitch length thereof) at lower temperatures.

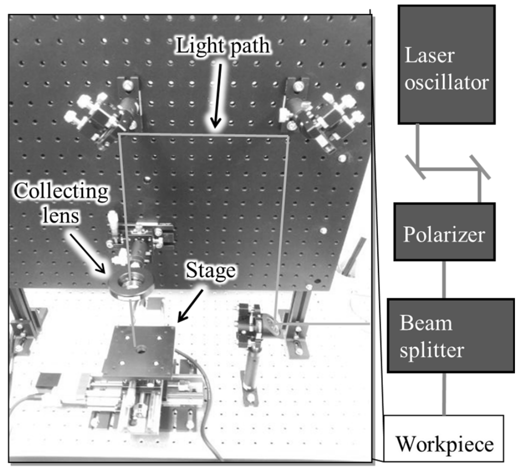

Fig. 8. Processing model of a short-pulsed laser.

4. Experiments

From the FDTD simulation results, we predicted the geometry of LIPSS at 20-ps pulse duration depending on the laser energy density and wavelength, and the low-temperature environment facilitated the fabrication of LIPSS with high aspect ratio. The experiments were then conducted to confirm the effects of both the pulse duration close to CRT and heat on the fabrication and geometry of LIPSS with the 20-ps pulsed laser while varying the laser-irradiation conditions.

4.1. Experimental Conditions

SUS304 substrates with mirror surfaces were prepared. Laser irradiation-experiments on the mirror surfaces were conducted using a picosecond-pulse laser oscillator (Ekspla, PL2250-50P20) with 20-ps pulse duration. The experimental setup is depicted in **Fig. 8**, including a polarizer, beam splitter, and collecting lens with the focusing range of 150 mm.

Table 2. Experimental conditions.

Wavelength	1064, 532, 355, 266 nm
Pulse duration	20 ps
Frequency	50 Hz
Pulse n	1–1000 pulse(s)
Energy density E_d	0.0034–4.47 J/cm^2
Temperature	223, 293 K
Workpiece	SUS304

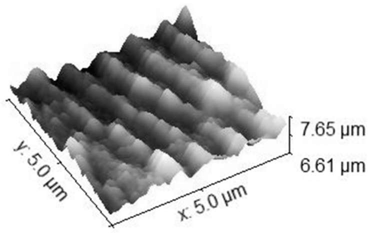

Fig. 9. AFM image of LIPSS at 1064-nm laser wavelength.

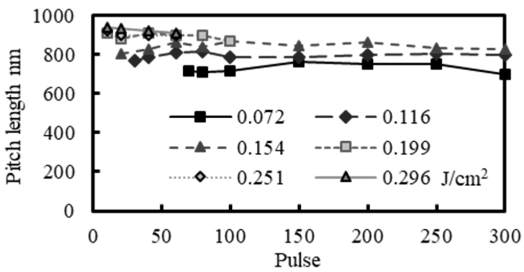

Fig. 10. Pitch length of LIPSS at 1064-nm wavelength.

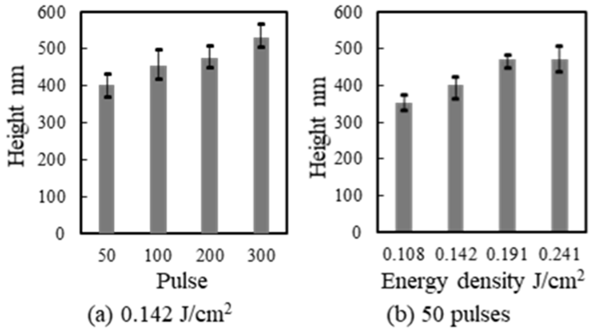

Fig. 11. Height of LIPSS at 1064-nm wavelength.

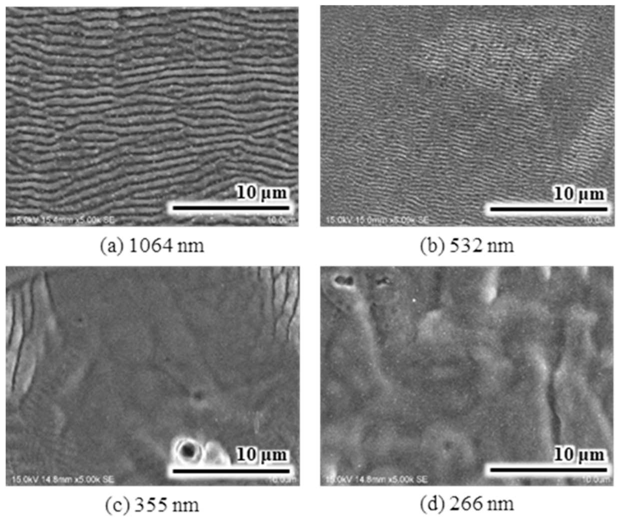

Fig. 12. SEM images of irradiated regions at different laser wavelength.

The laser-irradiation conditions are listed in **Table 2**. The laser with the Gaussian beam profile was irradiated on the substrate without scanning. The pulses and energy density were varied, and the laser wavelengths were set to 1064, 532, 355, and 266 nm. The material temperatures were set to 223 K and 293 K using a thermal controller for microscopy (Collet Kogyo Co., Ltd.). The workpiece was refrigerated on the holder in the controller, where liquid nitrogen flowed, and the laser was irradiated through a window in the vacuum. The central parts of the laser-irradiated regions were observed using a scanning electron microscope (SEM), a transmission electron microscope (TEM), and an atomic force microscope (AFM).

4.2. Experimental Results

4.2.1. Experiments with Various Energy Densities and Pulses at 1064-nm Laser Wavelength

In **Fig. 9**, we depict an example of the AFM image of LIPSS. In **Fig. 10**, we depict changes in the pitch length of LIPSS for various pulses and energy densities. The pitch length was approximately 700–900 nm and slightly increased upon increasing the energy density irrespective of pulses, as attributed to the parametric decay. In **Fig. 11**, we depict the changes in the height of LIPSS. The height of LIPSS was approximately 350–550 nm and slightly increased upon increasing the pulses and energy density. Overall, the pitch length and height of the LIPSS fabricated on SUS304 using the short-pulsed laser are approximately 700–900 and 350–550 nm, respectively. The aspect ratio of LIPSS (i.e., the height of LIPSS divided by the pitch length thereof) with the 20-ps pulsed laser is greater than that of LIPSS with ultrashort-pulsed lasers that, in the case of with the wavelength of 800 nm, fabricated LIPSS with approximately pitch length of 600 nm, height of 150–250 nm and aspect ratio of 0.25–0.42 on stainless steel surfaces [32–35] due to removal of convex parts with high intensity [13].

4.2.2. Experiments with Various Laser Wavelengths

In **Fig. 12**, we depict the SEM images of the laser-irradiated regions by using various laser wavelengths. The 1064- and 532-nm-wavelength lasers fabricated LIPSS, but the 355- and 266-nm-wavelength lasers did not fabricate LIPSS, while the ultrashort-pulsed laser with 370-fs pulse duration at 257-nm wavelength fabricated LIPSS [17]. It is considered that significant nonperiodic

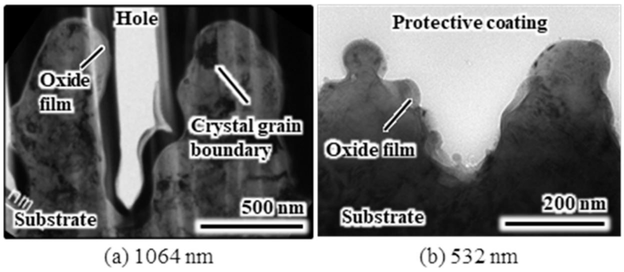

Fig. 13. TEM images of irradiated regions at 1064 and 532 nm laser wavelength.

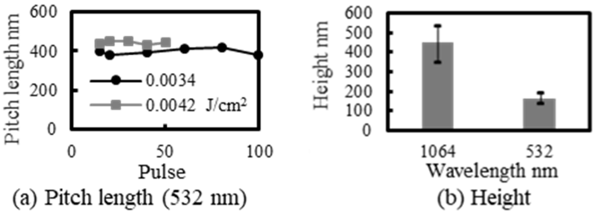

Fig. 14. Geometry of LIPSS at 532- and 1064-nm laser wavelength.

absorption, as mentioned in Section 3.3.2, occurs deeper in the case of 355- and 266-nm-wavelength lasers compared with the ultrashort pulsed laser, and the entire irradiated surface is removed. Additionally, the 532-nm-wavelength laser required lower energy density to fabricate LIPSS compared with the 1064-nm-wavelength laser, as the short-wavelength laser is absorbed deeper into the substrate.

In **Fig. 13**, we depict the TEM images of the cross sections of the LIPSS fabricated using the 1064- and 532-nm-wavelength lasers, respectively. The LIPSS with 10-μm thick oxide films were larger at 1064-nm laser wavelength than that at 532-nm laser wavelength. In **Fig. 14**, we depict the changes in the pitch length and height of LIPSS for each laser-irradiation condition, respectively. The pitch length and height of the 532-nm-wavelength laser fabricated LIPSS were initially approximately 400 nm and 200 nm, respectively. Both of them slightly increased upon increasing the energy density, as is the case of the LIPSS fabricated using the 1064-nm-wavelength laser.

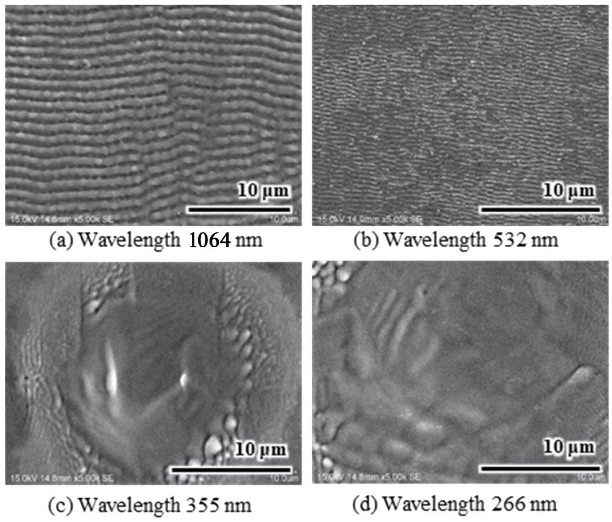

Fig. 15. SEM images of irradiated regions at 223 K.

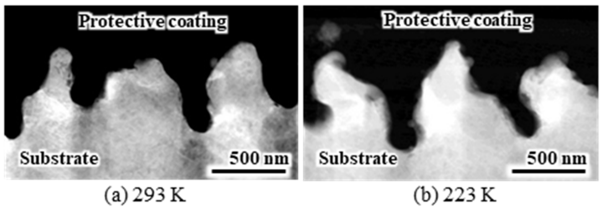

Fig. 16. TEM images of LIPSS at 1064-nm laser wavelength and various temperatures.

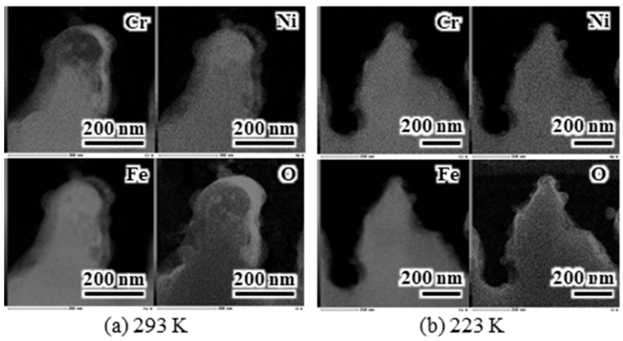

Fig. 17. Element mappings of TEM images LIPSS at 1064-nm laser wavelength and various temperatures.

4.2.3. Experiments with Various Material Temperatures

In **Fig. 15**, we depict the SEM images of the irradiated regions for low material temperature. The 1064- and 532-nm-wavelength lasers fabricated LIPSS, but 355- and 266-nm-wavelength lasers could not fabricate LIPSS even if the material temperature decreased. In **Fig. 16**, we depict the TEM images of LIPSS at 1064-nm wavelength and various temperatures. The LIPSS were sharp at 223 K, while they were roundish at 293 K. In **Fig. 17**, we depict the element mappings detected via energy dispersive X-ray spectrometry of the TEM images. The laser irradiation at low material temperature suppressed the growth of an oxide film without changing the other elements such as chromium, nickel, and iron, namely, the short-pulsed laser with 20-ps pulse duration exerted thermal influence for the fabrication of LIPSS, melting and producing roundish LIPSS. In **Fig. 18**, we depict the changes in the pitch length of LIPSS at 223 K. Similar to the case at 293 K, the pitch length of LIPSS at 223 K was approximately 800–1000 and 400 nm with the 1064- and 532-nm-wavelength lasers, respectively, while the LIPSS fabricated at higher temperature had longer pitch length [19, 21], as the change of 50 K was insufficiently small to change the pitch length of LIPSS. In **Fig. 19**,

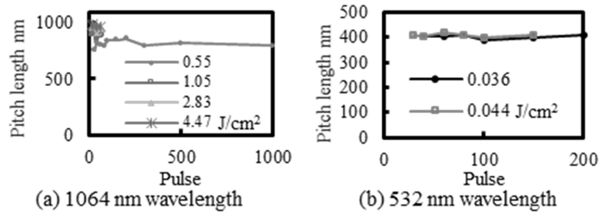

Fig. 18. Pitch length of LIPSS at 223 K.

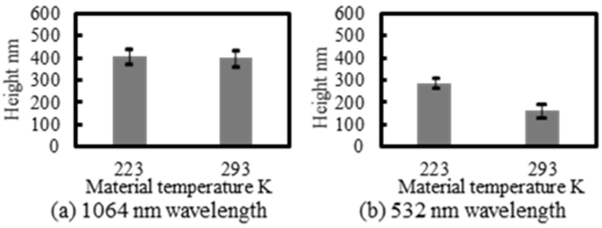

Fig. 19. Height of LIPSS for each material temperature.

we depict the changes in the height of LIPSS for each material temperature. The height of LIPSS at 223 K was greater than that at 293 K, as cooling material easily propagated surface plasmons and increased the ratio of the electric-field intensity at the bottom of groove to that at the top of groove. Accordingly, these results demonstrated the effects of pulse duration close to CRT and heat on the fabrication and geometry of LIPSS using the 20-ps pulsed laser. In addition, the results verified the efficiency of the short-pulsed laser and low-temperature environment to fabricate stably uniform LIPSS with high aspect ratio on the entire irradiated surface at low cost compared with the ultrashort pulsed laser, owing to the prevention of the removal of the convex parts of LIPSS because of low intensity of the 20-ps pulsed laser and to the extension of the CRT and the reduction of thermal effects by cooling material, causing dominant optical behavior.

5. Conclusions

We studied the effects of 20-ps pulse duration and heat on the electric-field-intensity distribution and resultant LIPSS to stably and effectively fabricate LIPSS on the entire irradiated surface. The following are the results of simulations and experiments performed using the 20-ps pulsed laser.

1. The pitch length and the height of the LIPSS fabricated on SUS304 using the short-pulsed laser at 1064-nm wavelength are 700–900 and 350–550 nm, respectively. The aspect ratio of LIPSS is approximately 0.5, which is greater than 0.2–0.4 of LIPSS fabricated using ultrashort-pulsed lasers.

2. The 355- and 266-nm-wavelength lasers could not fabricate LIPSS, as the electric-field intensity was high at both the top and bottom of the groove, following which significant nonperiodic absorption occurred deeper compared with the ultrashort pulsed laser, and, therefore, the entire irradiated surface was removed.

3. Compared with the ultrashort pulsed laser, the short pulsed laser experienced thermal influences, thereby producing roundish LIPSS with thick oxide films. The low-temperature environment suppressed the growth of oxide films and promoted the fabrication of LIPSS with high aspect-ratio because of the resultant extension of CRT, thereby facilitating the propagation of surface plasma waves and increasing the ratio of the electric-field intensity at the bottom of groove to that at the top of groove.

Acknowledgements

The authors would like to express their gratitude to the Kuriyagawa/Mizutani Laboratory at Tohoku University for supporting this research. This study was supported in part by JSPS KAKENHI under Grant Numbers JP17K06074 and JP17KK0126.

References:

[1] S. Mitrovic, D. Adamovic, F. Zivic, D. Dzunic, and M. Pantic, "Friction and wear behavior of shot peened surfaces of 36CrNiMo4 and 36NiCrMo16 alloyed steels under dry and lubricated contact conditions," Applied Surface Science, Vol.290, pp. 223-232, 2014.

[2] E. S. Kim, S. M. Kim, and Y. Z. Lee, "The effect of plateau honing on the friction and wear of cylinder liners," Wear, Vol.400, No.401, pp. 207-212, 2018.

[3] S. Shamsudin, M. Ahmad, A. Aziz, R. Fakhriah, F. Mohamad, N. Ahmad, N. Nafarizal, C. Soon, A. Ameruddin, A. Faridah, M. Shimomura, and K. Murakami, "Hydrophobic rutile phase TiO2nanostructure and its properties for self-cleaning application," AIP Conf. Proc., Vol.1883, 020030, 2017.

[4] Y. Tanaka, "Fabrication of Anti-reflective Structures Using Glass Molding," New Glass, Vol.23, No.4, pp. 32-38, 2008.

[5] J. Lu, M. P. Rao, N. C. MacDonald, D. Khang, and T. J. Webster, "Improved endothelial cell adhesion and proliferation on patterned titanium surfaces with rationally designed, micrometer to nanometer features," Acta Biomaterialia, Vol.4, pp. 192-201, 2008.

[6] K. Nakamura, Y. Nishitani, and T. Kitano, "Frictional properties of plants-derived polyamide against surface microstructures of metal counterpart fabricated by femtosecond laser," AIP Conf. Proc., Vol.1914, 200002, 2017.

[7] D. Chu, K. Yin, X. Dong, Z. Luo, and J. Duan, "Femtosecond laser fabrication of robust underwater superoleophobic and anti-oil surface on sapphire," AIP Advances, Vol.7, 115224, 2017.

[8] A. Y. Vorobyev and C. Guo, "Antireflection effect of femtosecond laserinduced periodic surface structures on silicon," Optics Express, Vol.19, No.5, pp. 1031-1036, 2011.

[9] T. Shinonaga, S. Kinoshita, Y. Okamoto, M. Tsukamoto, and A. Okada, "Formation of Periodic Nanostructures with Femtosecond Laser for Creation of New Functional Biomaterials," Procedia CIRP, Vol.42, pp. 57-61, 2016.

[10] M. Hashida, A. Semerok, O. Gobert, G. Petite, Y. Izawa, and J. Wagner, "Ablation threshold dependence on pulse duration for copper," Applied Surface Science, Vol.197, No.198, pp. 862-867, 2002.

[11] J. Yang, L. Pabst, W. Perrie, O. Allegre, G. Dearden, and S. P. Edwardson, "Advanced Laser Patterning for Security Marking of High Value Metal Components," Procedia Engineering, Vol.183, pp. 363-368, 2017.

[12] R. Harzic, D. Breitling, M. Weikert, S. Sommer, C. Föhl, S. Valette, C. Donnet, E. Audouard, and F. Dausinger, "Pulse width and energy influence on laser micromachining of metals in a range of 100 fs to 5 ps," Applied Surface Science, Vol.249, pp. 322-331, 2005.

[13] S. Kinoshita, T. Shinonaga, Y. Okamoto, and A. Okada, "Study on Shape Variation of Periodic Surface Nanostructures Produced with Ultrashort Pulse Laser for Control of Cell Spreading Direction," Proc. of Int. Conf. on Leading Edge Manufacturing in 21st Century (LEM21), 014, 2017.

[14] K. Mikami, S. Motokoshi, M. Fujita, T. Somekawa, T. Jitsuno, and K. Tanaka, "Temperature Dependences of Laser Induced Plasma Thresholds and Periodic Structures by Nanosecond Infrared Laser for Copper, Iron, and Chrome," Applied Physics Express, Vol.5, No.6, 062701, 2012.
[15] M. Hashida, Y. Ikuta, Y. Miyasaka, S. Tokita, and S. Sakabe, "Simple formula for the interspaces of periodic grating structures self-organized on metal surfaces by femtosecond laser ablation," Applied Physics Letters, Vol.102, 174106, 2013.
[16] T. Shinonaga, M. Tsukamoto, and G. Miyaji, "Periodic nanostructures on titanium dioxide film produced using femtosecond laser with wavelengths of 388 nm and 775 nm," Optics Express, Vol.22, No.12, pp. 14696-14704, 2014.
[17] F. Fraggelakis, G. Mincuzzi, I. Manek-Hönninger, J. Lopez, and R. Kling, "Rainer Generation of micro- and nano-morphologies on a stainless steel surface irradiated with 257 nm femtosecond laser pulses," RSC Advances, Vol.8, No.29, pp. 82-87, 2018.
[18] G. Deng, G. Feng, and S. Zhou, "Experimental and FDTD study of silicon surface morphology induced by femtosecond laser irradiation at a high substrate temperature," Optics Express, Vol.25, No.7, pp. 7818-7827, 2017.
[19] S. Gräf, C. Kunz, S. Engel, T. Derrien, and F. Müller, "Femtosecond Laser-Induced Periodic Surface Structures on Fused Silica: The Impact of the Initial Substrate Temperature," Materials, Vol.11, No.8, 1340, 2018.
[20] Y. Li, Q. Wu, M. Yang, Q. Li, Z. Chen, C. Zhang, J. Sun, J. Yao, and J. Xu, "Uniform deep-subwavelength ripples produced on temperature controlled LiNbO 3: Fe crystal surface via femtosecond laser ablation," Applied Surface Science, Vol.478, pp. 779-783, 2019.
[21] M. Mezera, J. Bonse, and G. Römer, "Influence of Bulk Temperature on Laser-Induced Periodic Surface Structures on Polycarbonate," Polymers, Vol.11, No.12, 1947, 2019.
[22] C. Wang, L. Jiang, F. Wang, X. Li, Y. Yuan, H. Xiao, H. Tsai, and Y. Lu, "First-principles electron dynamics control simulation of diamond under femtosecond laser pulse train irradiation," J. of Physics: Condensed Matter, Vol.24, No.27, 275801, 2012.
[23] M. Lebugle, N. Sanner, O. Utéza, and M. Sentis, "Guidelines for efficient direct ablation of dielectrics with single femtosecond pulses," Applied Physics A: Materials Science and Processing, Vol.114, pp. 129-142, 2014.
[24] S. Maruo, O. Nakamura, and S. Kawata, "Evanescent-wave holography by use of surface-plasmon resonance," Applied Optics, Vol.36, No.11, pp. 2343-2346, 1997.
[25] S. Sakabe, M. Hashida, S. Tokita, S. Namba, and K. Okamuro, "Mechanism for self-formation of periodic grating structures on a metal surface by a femtosecond laser pulse," Physical Review B, Vol.79, No.3, 033409, 2009.
[26] L. Gemini, M. Hashida, Y. Miyasaka, S. Inoue, J. Limpouch, T. Mocek, and S. Sakabe, "Periodic surface structures on titanium self-organized upon double femtosecond pulse exposures," Applied Surface Science, Vol.336, pp. 349-353, 2015.
[27] S. Kodama, S. Suzuki, A. Shibata, K. Shimada, M. Mizutani, and T. Kuriyagawa, "Effect of Crystal Structure on Fabrication of Fine Periodic Surface Structures with Short Pulsed Laser," Int. J. Automation Technol., Vol.12, No.6, pp. 868-875, 2018.
[28] S. Kodama, S. Suzuki, K. Hayashibe, K. Shimada, M. Mizutani, and T. Kuriyagawa, "Control of Short-Pulsed Laser Induced Periodic Surface Structures with Machining – Picosecond Laser Micro/Nanotexturing with Ultraprecision Cutting –," Precision Engineering, Vol.55, pp. 433-438, 2019.
[29] G. Miyaji and K. Miyazaki, "Ultrafast Dynamic Processes for Periodic Surface Nanostructure Formation lnduced with Femtosecond Laser Pulses," Laser Original, Vol.41, No.10, pp. 816-820, 2013.
[30] K. S. Yee, "Numerical solution of initial boundary value problems involving maxwell's equations in isotropic media," IEEE Trans. Antenna Propagation, Vol.14, No.3, pp. 302-307, 1966.
[31] O. Hashimoto, "Finite Difference Time Domain Method," Morikita Publishing, 2006.
[32] L. Qi, K. Nishii, and Y. Namba, "Regular subwavelength surface structures induced by femtosecond laser pulses on stainless steel," Opt. Lett., Vol.34, No.12, pp. 6-8, 2009.
[33] K. Kawahara and H. Sawada, "Coverage ratio increase of fluorine coatings on stainless steel by ultrashort pulse laser irradiation," JSPE Autumn Meeting, pp. 237-238, 2016.
[34] M. Martínez-Calderon, A. Rodríguez, A. Dias-Pontea, M. C. Morant-Minana, M. Gómez-Aranzadi, and S. M. Olaizola, "Femtosecond laser fabrication of highly hydrophobic stainless steel surface with hierarchical structures fabricated by combining ordered microstructures and LIPSS," Applied Surface Science, Vol.374, pp. 81-89, 2016.
[35] M. Martínez-Calderon, M. Manso-Silván, A. Rodríguez, M. Gómez-Aranzadi, J. P. García-Ruiz, S. M. Olaizola, and R. J. Martín-Palma, "Surface micro- and nano-texturing of stainless steel by femtosecond laser for the control of cell migration," Scientific Reports, Vol.6, No.1, 36296, 2016.

Name:
Shuhei Kodama

Affiliation:
Assistant Professor, Department of Mechanical Systems Engineering, Graduate School of Engineering, Tokyo University of Agriculture and Technology

Address:
6-311, 2-24-16 Nakacho, Koganei, Tokyo 184-0012, Japan

Name:
Keita Shimada

Affiliation:
Assistant Professor, Department of Mechanical Systems Engineering, Graduate School of Engineering, Tohoku University

Address:
6-6-01 Aramaki Aza-Aoba, Aoba-ku, Sendai, Miyagi 980-8579, Japan

Name:
Masayoshi Mizutani

Affiliation:
Associate Professor, Department of Mechanical Systems Engineering, Graduate School of Engineering, Tohoku University

Address:
6-6-01 Aramaki Aza-Aoba, Aoba-ku, Sendai, Miyagi 980-8579, Japan

Name:
Tsunemoto Kuriyagawa

Affiliation:
Professor, Bio-Medical Interface Fabrication Laboratory, Graduate School of Biomedical Engineering, Tohoku University

Address:
6-6-01 Aramaki Aza-Aoba, Aoba-ku, Sendai, Miyagi 980-8579, Japan